

Non-collinear Magnetic Order in the Double Perovskites: Double Exchange on a Geometrically Frustrated Lattice

Rajarshi Tiwari and Pinaki Majumdar
Harish-Chandra Research Institute,
Chhatnag Road, Jhusi, Allahabad 211019, India
(Dated: 28 April 2011)

Double perovskites of the form $A_2BB'O_6$ usually involve a transition metal ion, B, with a large magnetic moment, and a non magnetic ion B' . While many double perovskites are ferromagnetic, studies on the underlying model reveal the possibility of anti-ferromagnetic phases as well *driven by electron delocalisation*. In this paper we present a comprehensive study of the magnetic ground state and T_c scales of the minimal double perovskite model in three dimensions using a combination of spin-fermion Monte Carlo and variational calculations. In contrast to two dimensions, where the effective magnetic lattice is bipartite, three dimensions involves a geometrically frustrated face centered cubic (FCC) lattice. This promotes non-collinear ‘spiral’ states and ‘flux’ like phases in addition to collinear anti-ferromagnetic order. We map out the possible magnetic phases for varying electron density, ‘level separation’ $\epsilon_B - \epsilon_{B'}$, and the crucial $B'B'$ (next neighbour) hopping t' .

Keywords: double perovskite, double exchange, geometric frustration, non-collinear magnetism

I. INTRODUCTION

Double perovskites (DP) constitute a large family of materials¹ with molecular formula $A_2BB'O_6$, where A is an alkali or alkaline earth metal, and B and B' are typically transition metals. Although double perovskites have been studied for decades², the discovery of high T_c ferromagnetism and half-metallicity in Sr_2FeMoO_6 has led to renewed interest in their properties. Later, in a number of explorations it was discovered that these materials are candidates for various technological applications, *e.g.*, in spintronics³(Sr_2FeMoO_6), magneto-dielectrics^{4,5}(La_2NiMnO_6), and magneto-optics⁶(Sr_2CrOsO_6, Sr_2CrReO_6). Their properties are determined by the couplings on the B and B' ions, the B and B' valence state, and the structural order in the B- B' lattice.

The magnetism in the DP's arises from a combination of (i) Hund's coupling on the B, B' ions and (ii) electron delocalisation. While there are important DP's where both B and B' are magnetic ions, in the current work we will restrict ourselves to materials where only one ion, B, say, is magnetic. For example, in Sr_2FeMoO_6 (SFMO) the B atom (Fe) is magnetic while B' (Mo) is non magnetic⁷. Even in this restricted class, a large variety of compounds can be realized by taking 3d, 4d or 5d transition metals as B and B' , and various alkaline earths and rare-earths as A. These lead to a variety of properties, *e.g.*, high T_c ferro(or ferri) magnetism (FM), with half-metallic^{8,9} or insulating behavior¹⁰.

There have been several attempts at a theoretical understanding of the magnetism in these materials. These consist of (i) *ab initio* electronic structure calculations, and (ii) model Hamiltonian based approaches. The *ab initio* calculations⁵⁻⁷ provide material specific information about the electronic structure and allow a rough estimate of the T_c ¹¹. Unfortunately, these calculations are rather complicated for non-collinear magnetic phases

that are likely in a frustrated magnetic lattice, see Fig.1. In such situations model Hamiltonian studies can provide some insight on possible ordered states.

Early model calculations for double perovskites used dynamical mean field theory (DMFT) to estimate T_c and the magnetic stability window^{12,13}, focusing on ferromagnetism. Earlier work on the classical Kondo lattice¹⁴⁻¹⁷ had revealed that variation in carrier density can lead to a wide variety of phases in a spin-fermion problem. Indeed, calculation¹⁸ in a two dimensional (2D) model of double perovskites confirmed the existence of antiferromagnetic (AF), albeit collinear, phases. The ‘frustrated’ character of the three dimensional (3D) DP lattice raises the intriguing possibility of doping driven non collinear magnetic phases as well. Our study aims to explore this

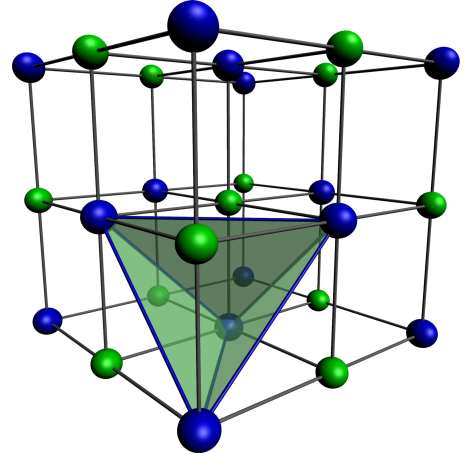


FIG. 1: Colour online: The structure of B- B' lattice in a cubic ordered double perovskite. The B and B' alternate (as in rock-salt) in the ordered structure. If the bottom corner (blue) atom is B, then its B nearest neighbours (connected by lines) are also nearest neighbours of each other. The triangles preclude a ‘G type’ antiferromagnetic phase.

issue in detail.

Our main results are the following. Using a combination of Monte Carlo and variational minimization, we map out the magnetic ground state (Fig.2) at large Hund's coupling for varying electron density and B-B' level separation. In addition to FM, and collinear A and C type order, the phase diagram includes large regions of non-collinear Flux and spiral phases and windows of phase separation. Modest B'B' hopping leads to significant shift in the phase boundaries, and "particle-hole asymmetry". We provide estimates of the T_c of these magnetic phases.

The paper is organized as follows. In Section II we describe the model and methods while Section III describes our results in the particle-hole symmetric case ($t' = 0$), and Section IV describes the effect of finite t' . Section V discusses our results in the general context of frustrated magnets and also their relevance for the real materials. Section VI concludes the paper.

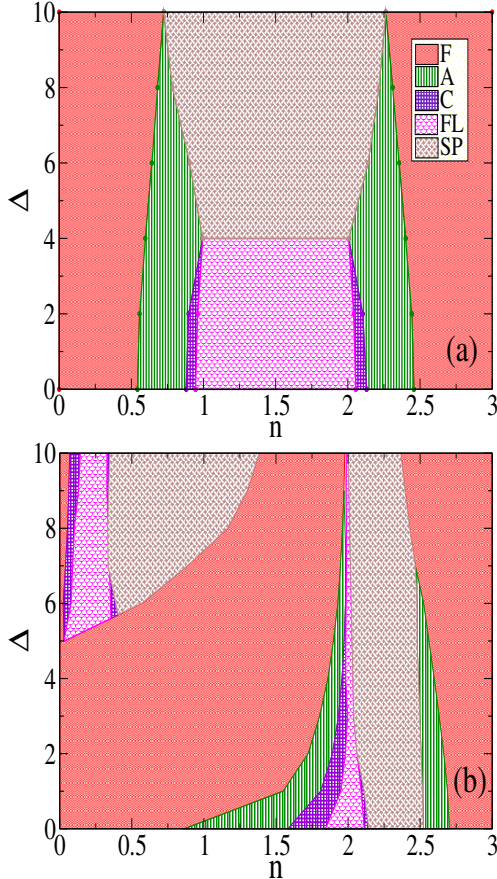


FIG. 2: Colour online: Magnetic ground state for varying electron density, n , and effective B-B' level separation, Δ . Top: phase diagram with only BB', *i.e.*, nearest neighbour, hopping. Bottom: phase diagram when an additional B'B' hopping, $t'/t = -0.3$, is included. The labels are: F (ferromagnet), A (planar phase), C (line like), FL (Flux) and SP (spiral). This figure does not show the narrow windows of phase separation in the model.

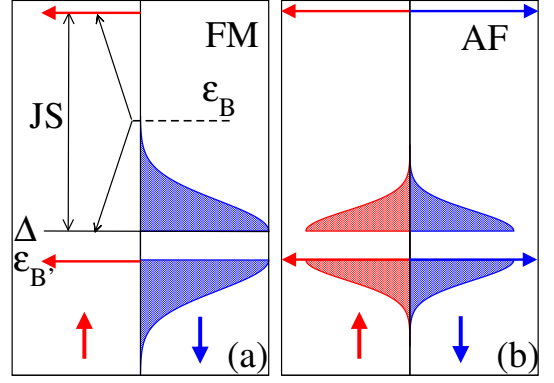


FIG. 3: Colour online: Schematic electronic structure for the DP model in the particle hole symmetric case. The left and right aligned arrows denote localised atomic levels. Red and blue denote \uparrow and \downarrow spins respectively. For FM (left figure) only one spin channel (say \downarrow) delocalises and forms a band, while other (say \uparrow) stays localise at 0. While in typical AF phases in the right figure arises, where the electron conduction paths get divided into two disjoint sub-lattices, in each of which one spin channel conducts while other remains localised at 0.

II. MODEL AND METHOD

Previous study of double perovskites in two dimensions²⁰ revealed three collinear phases, namely FM, a diagonal stripe phase (FM lines coupled antiferromagnetically) and a 'G type' phase (up spin surrounded by down and *vice versa*). In 2D the B sub-lattice is square and bipartite, so there is no frustration. In a 3D *simple cubic* B lattice the counterparts of the 2D phases would be FM, A type (planar), C type (line like) and G type. The magnetic lattice in the DP's however, is FCC which is *non-bipartite*, so while one can construct FM and planar A type phases, the C type phase is modified and the G type phase cannot exist.

Fig.1 briefly indicates why it is impossible to have an 'up'(\uparrow) B ion to be surrounded by only 'down'(\downarrow) B ions, *i.e.*, the G type arrangement. Two B neighbours of a B ion are also neighbours of each other, frustrating G type order. The suppression of the G type phase, which occupies a wide window in 2D, requires us to move beyond collinear phases in constructing the 3D phase diagram. We will discuss the variational family in Section II C.

A. Model

The alternating arrangement of B and B' ions in the ordered cubic double perovskites is shown in Fig.1. We use the following one band model on that structure:

$$H = \epsilon_B \sum_{i \in B} f_{i\sigma}^\dagger f_{i\sigma} + \epsilon_{B'} \sum_{i \in B'} m_{i\sigma}^\dagger m_{i\sigma} - \mu \hat{N} - t \sum_{\langle ij \rangle} f_{i\sigma}^\dagger m_{j\sigma} + J \sum_{i \in B} \mathbf{S}_i \cdot f_{i\alpha}^\dagger \vec{\sigma}_{\alpha\beta} f_{i\beta}$$

The f^\dagger correspond to the B ions and the m^\dagger to the B'. ϵ_B and $\epsilon_{B'}$ are 'onsite' energy on the B and B' sites respectively, *e.g.*, the t_{2g} level energy of Fe and Mo in SFMO. μ is the chemical potential and $\hat{N} = \sum_{i\sigma} (f_{i\sigma}^\dagger f_{i\sigma} + m_{i\sigma}^\dagger m_{i\sigma})$ is the total electron number operator. t is the hopping amplitude between nearest neighbour B and B' ions. We augment this model later to study first neighbour B'B' hopping t' as well. J is the (Hund's) coupling between the B core spin and the f conduction electron. We will use $|\mathbf{S}_i| = 1$, and absorb the magnitude of \mathbf{S} in J . $\sigma_{\alpha\beta}^\mu$ are the Pauli matrices.

The model has parameters J , ϵ_B , $\epsilon_{B'}$, and μ (or electron density). Since only the level difference matters, we set $\epsilon_{B'} = 0$. We have set $t = 1$, and use $J/t \gg 1$ so that the conduction electron spin at the B site is slaved to the core spin orientation. However, to keep the *effective* level difference between B and B' sites finite we use the parameter $\Delta = \epsilon_B - J$, and explore the phases as a function of n and Δ/t . We will present results for $t'/t = 0$

and ± 0.3 .

A schematic for the levels is shown in Fig.3. The structural unit cell of the system has 2 (one B, one B') atoms, which amounts to 4 atomic levels (2 up spin, 2 down spin). The two spin levels at the B site are separated by JS and overlap with 2 spin degenerate levels of the B' site at $\epsilon_{B'} = 0$. We take the large J limit, and take $\epsilon_B = JS/2 + \Delta$ with Δ in the range (0-10). One B band become centered at Δ and second goes to $JS + \Delta$. In this situation the down spin B and two B' bands overlap while up spin B band is always empty. The relevant electron density window includes the lowest three bands, so our electron density will be in the range $[0, 3]$.

To get a general feel of the band structure of the particle hole symmetric case, we notice that we have three levels (excluding the highest f_\uparrow level at $2J + \Delta$ which remains empty and is redundant for our purpose) in atomic limit. These include one spin slaved f_\downarrow level at Δ , and the two m_\uparrow , m_\downarrow , levels which overlap with the f_\downarrow levels depending on the spin configurations. This overlap leads

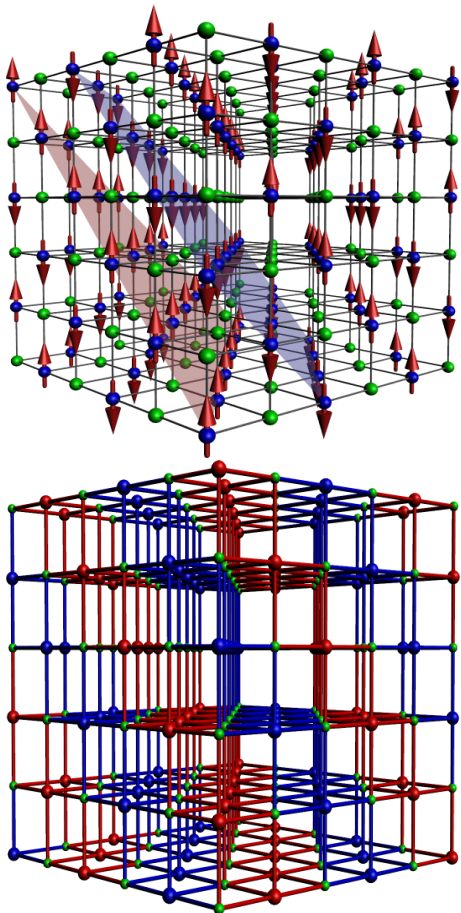


FIG. 4: Colour online. Top: Spin configuration for 'A type' order. The spins are parallel within the 111 planes (shown) and are antiparallel between neighbouring planes. Bottom: The differently coloured bonds show the electron delocalisation pathway for up and down spin electrons in the A type phase. The delocalisation is effectively two dimensional.

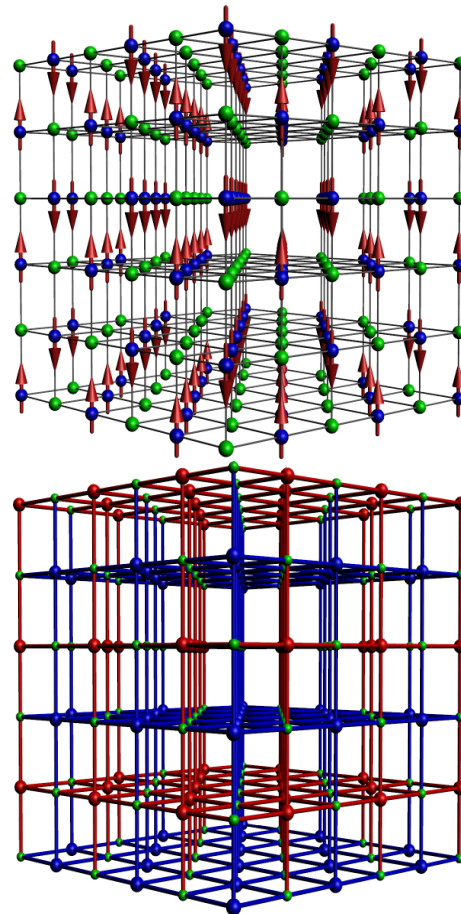


FIG. 5: Colour online. Top: Spin configuration in the 'C type' phase. Core spins are parallel on alternating 110 planes, and antiparallel on neighbouring planes. Bottom: the delocalisation path, consisting of the 110 planes and the horizontal 001 planes.

to electron delocalisation and band formation.

For the FM (left part in Fig.3), only one spin channel (say m_\downarrow) gets to delocalise through f sites and forms two bands, separated by a band gap of Δ , while other spin channel (say m_\uparrow) is localised at 0.

For collinear AF configurations (right part in Fig.3) the conduction path gets divided into two sub-lattices, such that each spin channel gets to delocalise in one sub-lattice (in which all the core spins point in same direction, making the ‘sub-lattice’ ferromagnetic. See Fig.4, and Fig.5 for the details of the conduction path). In one such sub-lattice, only one of the \uparrow or \downarrow delocalised, the other remains localised. The roles of \uparrow and \downarrow are reversed in going from one sub-lattice to other, as a result one gets spin-degenerate localised and dispersive bands for AF phases.

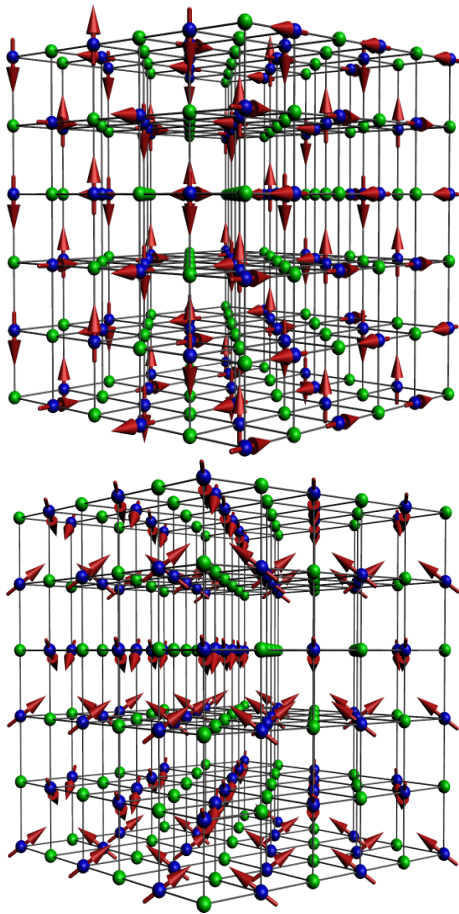


FIG. 6: Colour online. Spin configuration for a typical spiral phase (top) and the Flux phase (bottom). Since the spin configurations are non-collinear the electrons delocalise over the whole system.

B. Monte Carlo method

The model involves spins and fermions, and if the spins are ‘large’, $2S \gg 1$, they can be approximated as classical. This should be reasonable in materials like SFMO where $S = 5/2$. Even in the classical limit these spins are annealed variables and their ground state or thermal fluctuations have to be accessed via iterative diagonalisation of the electronic Hamiltonian. We use a real space Monte Carlo (MC) method where the cost of a spin update is estimated via a small cluster Hamiltonian instead of diagonalising the whole system¹⁹.

We typically use a $12 \times 12 \times 12$ system with the energy cost of a move estimated via a 4^3 cluster built around the reference site. We principally track the magnetic structure factor

$$S(\mathbf{q}) = \frac{1}{N^2} \sum_{\mathbf{r}, \mathbf{r}'} \langle \mathbf{S}_{\mathbf{r}} \cdot \mathbf{S}_{\mathbf{r}'} \rangle e^{i\mathbf{q} \cdot (\mathbf{r} - \mathbf{r}')}$$

where $\langle \dots \rangle$ denote thermal average.

Although the magnetic lattice is FCC, the electrons delocalise on the combined B-B’ system which is a cubic lattice. Hence we define our wave-numbers \mathbf{q} with respect to the full B-B’ lattice. As a result even a simple state like the ferromagnet corresponds to peaks at $\mathbf{q} = (0, 0, 0)$ and $\mathbf{q} = (\pi, \pi, \pi)$ and not just $\mathbf{q} = (0, 0, 0)$. This is because the spin field is also defined on B’ sites and it has to have zeros on these sites.

This complication, and the possibility of spiral phases, *etc*, mean that (i) there are multiple \mathbf{q} values which could be significant at low temperature, and (ii) the $S(\mathbf{q})$ peaks could be small even in the ordered state. Combined with the intrinsic noise in MC data (which is enhanced due to a complex energy landscape, discussed later) it is sometimes difficult to identify complicated ordered phases. Therefore, to complement the MC results we have also used the following variational scheme.

C. Variational scheme

We explore a set of magnetic states, comparing their energy to locate the minimum within that family for a fixed set of electronic parameters. We use:

$$\mathbf{S}_{\mathbf{r}} = p(\mathbf{r}) \{ \hat{x} \sin \theta(\mathbf{r}) \cos \phi(\mathbf{r}) + \hat{y} \sin \theta(\mathbf{r}) \sin \phi(\mathbf{r}) + \hat{z} \cos \theta(\mathbf{r}) \}$$

where $\theta(\mathbf{r}) = \mathbf{q}_\theta \cdot \mathbf{r}$ and $\phi(\mathbf{r}) = \mathbf{q}_\phi \cdot \mathbf{r}$ with $p(\mathbf{r}) = 1$ if $\mathbf{r} \in B$ and $p(\mathbf{r}) = 0$ if $\mathbf{r} \in B'$.

The vector field $\mathbf{S}_{\mathbf{r}}$ is characterized by the two wave-vectors \mathbf{q}_θ and \mathbf{q}_ϕ . For a periodic configuration, these should be $\mathbf{q}_\theta = \frac{2\pi}{L}(q_1, q_2, q_3)$ and $\mathbf{q}_\phi = \frac{2\pi}{L}(p_1, p_2, p_3)$, where q_i ’s and p_i ’s are integers, each of which take L values in $\{0, 1, 2, 3, \dots, L-1\}$. There are $\sim L^6$ ordered magnetic configurations possible, within this family, on a simple cubic lattice of linear dimension L .

Phase	Peak location in $S(\mathbf{q})$
Ferromagnet (FM)	$(0,0,0), (\pi, \pi, \pi)$
A-type antiferromagnet (A)	$(\frac{\pi}{2}, \frac{\pi}{2}, \frac{\pi}{2}), (\frac{3\pi}{2}, \frac{3\pi}{2}, \frac{3\pi}{2})$
C-type antiferromagnet (C)	$(0,0,\pi), (\pi, \pi, 0)$
Flux (FL)	$(\pi, 0, 0), (0, \pi, 0), (0, 0, \pi), (\pi, \pi, 0), (\pi, 0, \pi), (0, \pi, \pi)$
$\uparrow\uparrow\downarrow$ phase	$(\frac{\pi}{2}, 0, 0), (\frac{3\pi}{2}, 0, 0), (\frac{\pi}{2}, \pi, \pi), (\frac{3\pi}{2}, \pi, \pi)$
$\text{SP}_1 (\mathbf{q}_\theta, \mathbf{q}_\phi) = (0, \frac{\pi}{2}, \pi), (0, 0, 0)$	$(0, \frac{\pi}{2}, \pi), (\pi, \frac{\pi}{2}, 0), (0, \frac{3\pi}{2}, \pi), (\pi, \frac{3\pi}{2}, 0)$
$\text{SP}_2 (\mathbf{q}_\theta, \mathbf{q}_\phi) = (0, \frac{\pi}{2}, \pi), (0, \frac{\pi}{2}, 0)$	$(0, \frac{\pi}{2}, \pi), (\pi, \frac{\pi}{2}, 0), (0, \frac{3\pi}{2}, \pi), (\pi, \frac{3\pi}{2}, 0)$ $(0, 0, \pi), (\pi, 0, 0) + (\pi, \pi, 0) + (0, \pi, \pi)$
$\text{SP}_3 (\mathbf{q}_\theta, \mathbf{q}_\phi) = (0, \frac{\pi}{2}, \pi), (\frac{\pi}{2}, 0, \frac{\pi}{2})$	$(0, \frac{\pi}{2}, \pi), (\pi, \frac{\pi}{2}, 0), (0, \frac{3\pi}{2}, \pi), (\pi, \frac{3\pi}{2}, 0)$ $(\frac{\pi}{2}, \frac{\pi}{2}, \frac{3\pi}{2}), (\frac{3\pi}{2}, \frac{3\pi}{2}, \frac{\pi}{2}), (\frac{\pi}{2}, \frac{3\pi}{2}, \frac{3\pi}{2}), (\frac{3\pi}{2}, \frac{\pi}{2}, \frac{\pi}{2})$

TABLE I: Candidate phases, the associated $\mathbf{q}_\theta, \mathbf{q}_\phi$, and the peak locations in the structure factor $S(\mathbf{q})$.

The use of symmetries, *e.g.*, permuting components of \mathbf{q}_θ , *etc.*, reduces the number of candidates somewhat, but they still scale as $\sim L^6$. For a general combination of $\mathbf{q}_\theta, \mathbf{q}_\phi$ the eigenvalues of H cannot be analytically obtained because of the non trivial mixing of electronic momentum states. We have to resort to a real space diagonalisation. The Hamiltonian matrix size is $2N (= 2L^3)$ and the diagonalization cost is $\sim N^3$. So, a comparison of energies based on real space diagonalisation costs $\sim N^5$, possible only for $L \leq 8$.

We have adopted two strategies: (i) we have pushed this ' $\mathbf{q}_\theta, \mathbf{q}_\phi$ ' scheme to large sizes via a selection scheme described below, and (ii) for a few collinear configurations, where Fourier transformation leads to a small matrix, we have compared energies on sizes $\sim 400^3$.

First, scheme (i). For $L = 8$ we compare the energies of all possible phases, to locate the optimal pair $\{\mathbf{q}_\theta, \mathbf{q}_\phi\}_{min}$ for each μ . We then consider a larger system with a set of states in the neighbourhood of $\{\mathbf{q}_\theta, \mathbf{q}_\phi\}_{min}$. If we consider $\pm\pi/L$ variation about each component of \mathbf{q}_θ , *etc.*, that involves 3^6 states. The shortcoming of this method is that it explores only a restricted neighbourhood, dictated by the small size result. We have used $L = 12, 16, 20$ within this scheme.

The phases that emerge as a result of the above process are (i) Ferromagnet (FM), (ii) A-type, (iii) C-type, (iv) Flux, and (v) three spirals $\text{SP}_1, \text{SP}_2, \text{SP}_3$. A-type is consists of $(1, 1, 1)$ FM planes with alternate planes having opposite spin orientation (see Fig.4 top panel). If we convert each of these planes to alternating FM lines, so that the overall spin texture is alternating FM *lines* in all directions, we get C-type phase (see Fig.5).

The Flux phase is different from the spiral families described using period vectors $\mathbf{q}_\theta, \mathbf{q}_\phi$. It is the augmented version of Flux phase used in cubic lattice double exchange model by Alonso *et al*¹⁶(Table-I). It has spin-ice like structure, and is described by

$$S(\mathbf{r}) = \frac{p(\mathbf{r})}{\sqrt{3}}((-1)^{y+z}, (-1)^{z+x}, (-1)^{x+y})$$

The spiral SP_i phases are characterised by comensurate values of $\mathbf{q}_\theta, \mathbf{q}_\phi$ (See Table I for details of periods and the $S(\mathbf{q})$ peaks).

The simplest, SP_1 can be viewed as $\frac{\pi}{2}$ -angle pitch in the $(110), (101)$ and (011) directions. The other two spirals SP_2 SP_3 are respectively C-type and A-type modu-

lations upon SP_1 . Just as flipping alternate $1, 1, 1$ planes in a FM leads to the A type phase, flipping the spins in the (111) planes alternatively in SP_1 , leads to SP_3 . Analogously, flipping FM lines in a FM and leads to C-type order- and a similar exercise on SP_1 leads to SP_2 . This modulation is also seen in the $S(\mathbf{q})$ peaks of SP_2 and SP_3 . See the Table I, where all the three spirals have 4 $S(\mathbf{q})$ peaks common, and SP_2 and SP_3 possess extra $S(\mathbf{q})$ peaks of the A-type and C-type correlations.

In scheme (ii) we take collinear phases from the phase diagram via Monte-Carlo and variational scheme (i), and compare them on very large lattices. This does not require real space diagonalisation. The simple periodicity of these phases leads to coupling between only a few $|\mathbf{k}\rangle$ states. The resulting small matrix can be diagonalized for the eigenvalues and these summed numerically. We also did it for the Flux phase, where the resulting matrix is a bit larger, but still it gets us access to eigenvalues for the Flux phase on large lattices. The details of this calculation are discussed in Appendix A. Where the collinear phases (and Flux) seem to dominate the phase diagram we compute phase boundaries by calculating the energy on very large lattices.

III. PARTICLE-HOLE SYMMETRIC CASE

We first discuss the case of particle-hole symmetry, *i.e.*, $t' = 0$, and then the case of $t' \neq 0$. For each of these cases we first discuss the MC results, since these are unbiased, though affected by finite size and the cluster update mechanism. This provides a feel for the relevant candidate states that we can explore more carefully within a variational scheme. It also provides an estimate of T_c , not readily available within the variational scheme.

Following this we show the ground states and phase separation (PS) windows that emerge from the variational calculation for varying n and Δ/t . We also provide an alternate estimate of the " T_c " of these phases by calculating the energy difference $\delta E(n) = (E_{pm}(n) - E_{ord}(n))/N_s$, that the system gains via magnetic ordering. Here E_{pm} is the electronic energy averaged over disordered (paramagnetic) spin configurations while E_{ord} is the energy of the magnetically ordered ground state, both at the same electron density n . $N_s (= \frac{N}{2})$ is the number of spins in the system. The phases that dominate the

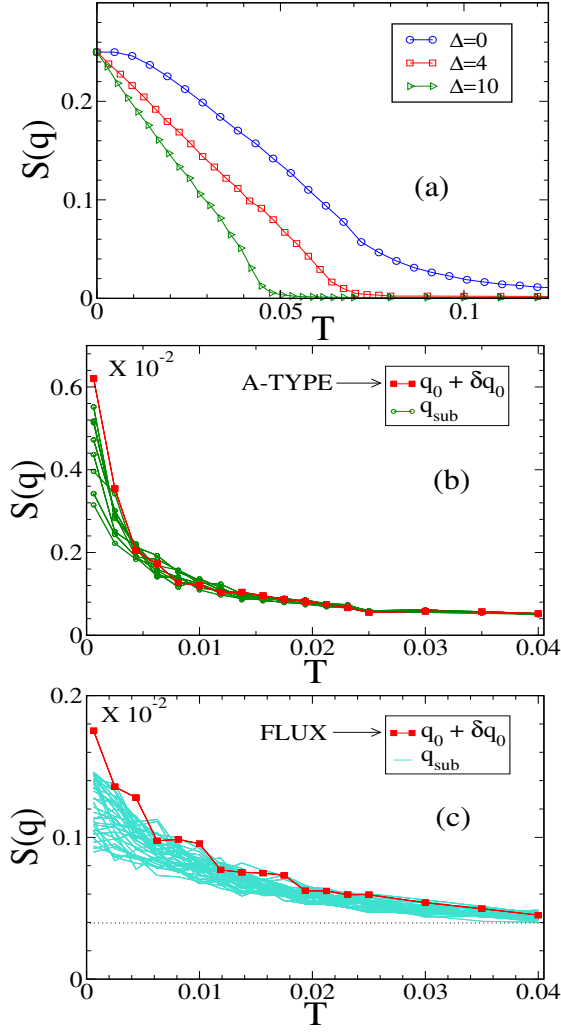


FIG. 7: Colour online: Temperature dependence of structure factor peaks for three typical densities and $t' = 0$. (a). For $\Delta = 0, 4, 10$, ferromagnetic order at $n = 0.20$. (b). The growth of A type correlations (and the noise around the principal peak, at $n = 0.50$). The ordering wave-vector \vec{q}_0 is listed in Table-I. $\delta\vec{q}_0$ are $\sim \mathcal{O}(\frac{1}{L})$ (c). Flux type correlations at $n = 1.50$. The features are at and around the ordering wave-vector in Table-I. Note the scale factors on the y axis in (b) and (c).

phase diagram are listed in Table-I, with the associated $\mathbf{q}_\theta, \mathbf{q}_\phi$, and the peak locations in the structure factor.

A. Monte Carlo

We studied a $N = 12^3$ system using the cluster based update scheme. We used a large but finite J to avoid explicitly projecting out any electronic states²², since that complicates the Hamiltonian matrix but allows only a small increase in system size. The magnetic phases were explored for $\Delta = 0, 4$ and 10 . An illustrative plot of peak features in $S(\mathbf{q})$ as function of temperature T , is

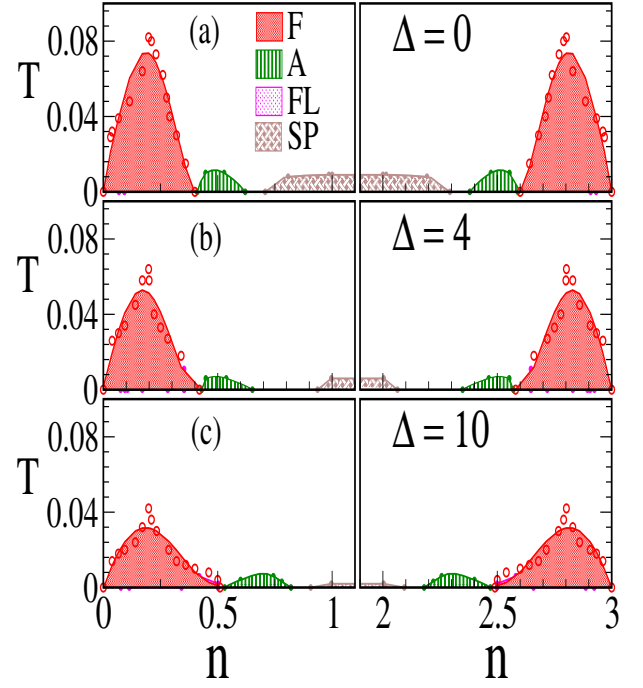


FIG. 8: Colour online: $n - T_c$ diagram for $\Delta = 0, 4, 10$ (top to bottom rows) as estimated from the Monte Carlo. Starting from low density ($n = 0$) towards high density ($n = 1$), we find FM with high T_c , thin window of A-type with very low T_c as compared to FM, followed by Flux in $\Delta = 0$ and ‘spiral’ in larger Δ case. The symbols are the actual MC estimated T_c , while the smooth lines are fit to the data.

shown in Fig.7 for some typical densities, where, for FM, $S(\mathbf{q}_{FM})$ shows monotonic decrease of T_c with increasing Δ . For A-type and Flux phase, the $S(\mathbf{q})$ data shows a number of sub-dominant \mathbf{q} peaks whose number keeps increasing as we move to more complicated phases with increasing density.

Using the structure factor data, we establish the $n - T_c$ phase diagram for $\Delta = 0, 4, 10$ that is plotted in Fig.8. The Monte Carlo captures mainly three collinear phases, namely FM, A-type, and a $\uparrow\uparrow\downarrow\downarrow$ phase. The $\uparrow\uparrow\downarrow\downarrow$ phase corresponds to two FM up planes followed by two FM down planes and so forth. As the carrier density is increased via increasing μ , we find a FM phase followed by the A-type AF. A $\uparrow\uparrow\downarrow\downarrow$ phase appears in a thin window surrounded by FM itself. We suspected that this as a finite size effect, and a comparison with the energy of the FM on larger lattices (20^3), shows that the FM is indeed the ground state in the thermodynamic limit, and so we consider FM and $\uparrow\uparrow\downarrow\downarrow$ collectively as FM only, and presence of $\uparrow\uparrow\downarrow\downarrow$ is not indicated in the phase diagram.

The FM is stable in the wings of band, and its stability window is enhanced as we increase Δ . The T_c however decreases with increasing Δ since the degree of B-B’ mixing (and kinetic energy) decreases.

With further increase in n the 2D system is known to make a transition to a line-like phase, and then a ‘G type’

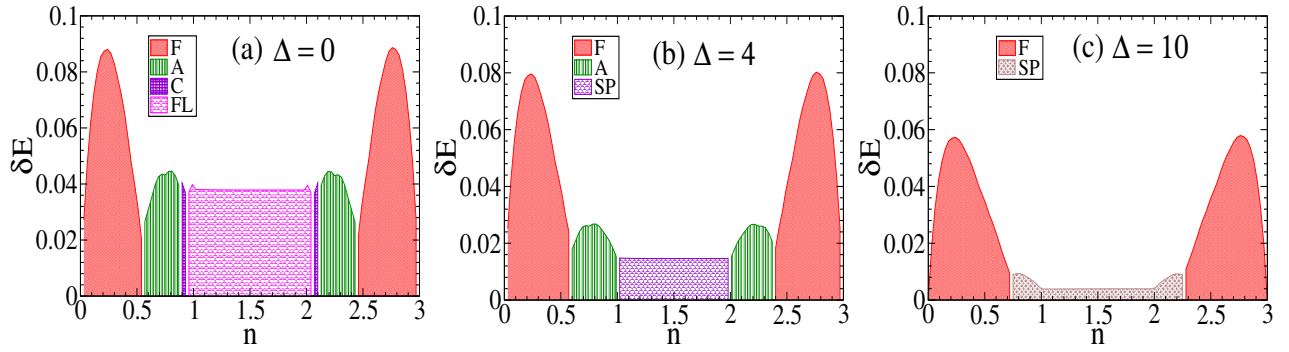


FIG. 9: Colour online: The energy difference δE of ground-state and paramagnetic phase. A variational estimate of the T_c for three values of (a) $\Delta = 0$, (b) $\Delta = 4$, (c) $\Delta = 10$ and $t' = 0$. The sequence of phases from low density to middle is FM, A, C and Flux ($\Delta = 0$) or spiral ($\Delta = 4, 10$). The decrease in the ' T_c ' with Δ is more drastic in AF phases.

phase (up spin surrounded by down, etc). In 3D one would expect the FM to change to a 'planar' (A type) phase, then a 'line like' (C type) phase and finally to a G type phase if possible. All of these are of course collinear phases, and geometric constraints may lead to non-collinear order as well.

While we do access the A type phase with some difficulty, our Monte Carlo cannot access the long range ordered C type phase. However, we see clear evidence of C type correlations in the structure factor. Comparing the energy of the ideal C type phase with the short range correlated phase that emerges from the MC we infer that such order is indeed preferred. However, we cannot estimate a reliable T_c scale. In the next section we will see that the variational calculation confirms the stability of the C type, among collinear phases, in this density window, and will get a rough estimate of the T_c from the energy δE .

The G type phase is geometrically disallowed on the B sub-lattice due to its FCC structure. An examination of the structure factor in the density window $n = [1, 2]$ suggests Flux like correlations at small Δ which evolves into a spiral at larger Δ . The frustration reduces the T_c of the phases in this density window compared to that of the FM. A comparison with the 2D result, where the system is unfrustrated, highlights the impact of frustration. In 2D, the ratio $T_c^{AF}/T_c^{FM} \lesssim 1$, while in 3D $T_c^{AF}/T_c^{FM} \lesssim 0.1$. If we compare the $(\delta E)^{AF}/(\delta E)^{FM}$ for 2D and 3D, the numbers come out to be ~ 1.1 and 0.5 respectively²³. The comparisons suggest a significant decrease in the binding energy (and hence T_c) of the AF phases relative to the FM as we move from 2D to 3D.

When $t' = 0$, the electron delocalisation happens through B-B'-B paths only (see the conduction paths, for example of collinear phases A and C in Fig.4 and 5 respectively). In this case all the phases have an atomic level located at $\epsilon_{B'}(=0)$ in the limit $J \rightarrow \infty$. This is directly seen in the density of states (DOS) of these phase. In Fig.10 we show the DOS for the F, A, C, Flux and paramagnet phases. This dispersion-less level gives con-

stant T_c in density region $n = [1, 2]$. This feature, and several others, are modified by finite B/B' hopping, which leads to broadening of this level. It makes the DOS of the various magnetic phases asymmetric (in energy) and also destroys the particle-hole symmetry in the phase diagram.

B. Variational scheme

Using the approach discussed earlier, we found the ground state configurations at different electron densi-

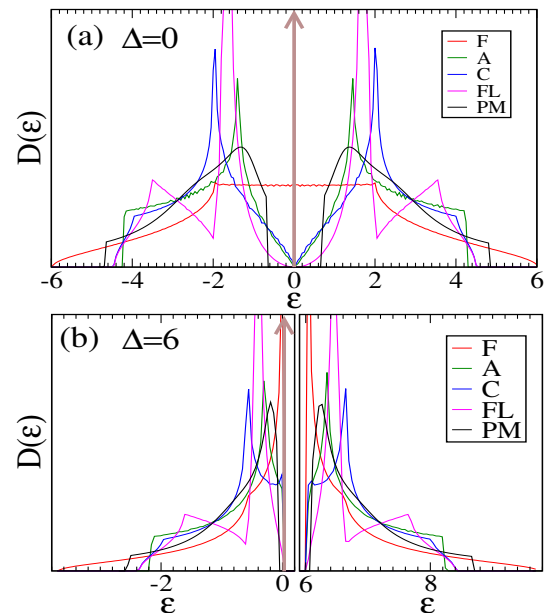


FIG. 10: Colour online: density of states for the F,A,C,FL (Flux) and PM (paramagnetic) phases. (a) for $\Delta = 0$ and (b) for $\Delta = 6$. In order of decreasing band width are phase F,PM,C,FL, and A (FL and C have same bandwidth). This is for both $\Delta = 0, 6$, and the order in general doesn't depend on the Δ

ties. In this set we also get certain spiral phases, which are small variations of FM, A, and C phases in the left and right part of the density window. Since in these parts Monte Carlo also gives (for FM, A) clean result, we interpret it as a finite size effect. To get convinced about it, we compare the energies of these collinear phases (FM, A, C) with all their neighboring modulations $\delta\vec{q}$ s, at various lattice sizes. We find that with increasing lattice size, the per particle energy difference between collinear phase, and lowest energy candidate with the neighboring $\mathbf{q}_\theta, \mathbf{q}_\phi$, decreases, which convinces us that if we go to large enough lattice size, this difference will eventually vanish and the collinear phases (F,A,C) will be the relevant candidates.

We use the similar scheme for the middle part, however there no simple phase is suggested by this variational scheme (neither by Monte Carlo). The phases we propose for the middle density part based on this variational scheme are SP_1 , SP_2 , SP_3 , and Flux. See the configurations in Fig.6 and $S(\mathbf{q})$ details from Table I.

In Fig.2, the magnetic ground state phase diagram is shown for $t' = 0$ and $t' = 0.3$ (top and bottom). We see that for $t' = 0$ the phase diagram is symmetric in density. For small Δ , in the range $0 - 4$, we have FM, followed by A-type, C-type, and Flux phase. The order reverses as we go in the other half of the density window. The G-type phase which was largest stable phase in 2D (Fig.2 and Fig.5 in Ref.¹⁸) is almost taken over by the Flux phase. The stability of the Flux phase decreases with Δ and it does not show up for $\Delta > 4$.

In Fig.10, we show the DOS for F, A, C, Flux and PM phases. The upper and the lower panel correspond to $\Delta = 0$ and $\Delta = 6$ respectively. In all the phases, at all Δ , there is a spike (delta function) at $\epsilon = 0$, which accounts for the non-dispersive level at $\epsilon_{B'} = 0$.

For FM all the core spins are \uparrow (say), so only \downarrow spin electrons from B' site get to delocalise while \uparrow spin electrons remain localised at $\epsilon = 0$, which corresponds to the localised band in the spectrum and the spike in the DOS. So the localised level in FM is an \uparrow spin level. The nature of this localised level however changes when we go to AF phases. In collinear phases, its easy to understand the nature of this localised band. Take for example the case of A-type in Fig.4 down panel with conduction path. The lattice is divided into two sublattices (each of which are of layered zigzag shape), blue and red, such that, if (say) core spins in the f sites in the blue sub-lattice are all \uparrow , then the same in red sub-lattice are \downarrow . As a result, in the blue sub-lattice, \downarrow spin electrons get to delocalise, while \uparrow spin electron remain localised. the opposite happens in the red sub-lattice. Since these lattices are disconnected from each other, one can separately diagonalise them. But each of this sub-lattice, however complicated in shape, is a FM, so it gives $\frac{1}{3}$ of the levels localised at $\epsilon = 0$, which will be \uparrow spin in blue sub-lattice, while it will be \downarrow spin in red sublattice. Since both the sub-lattices have same number of sites/unit cells, we get $\frac{1}{3}$ of the levels localised at $\epsilon = 0$ but now spin degenerate. The

delocalised states have also to be spin-degenerate, and their nature depends on the way the conduction paths divide the lattice into two sub-lattices.

For each spin channel the conduction paths are layered zigzag, 2 dimensional in the A type phase, while they are 3 dimensional in the C type phase.

This appearance of the localised band is not restricted to just the collinear phases, but also happens for non-collinear phases, and even the paramagnet.

Explain where the localised level arises from in generic magnetic structures, including the paramagnet.

IV. PARTICLE-HOLE ASYMMETRY

The model with only ‘nearest neighbour’ (BB’) hopping has a rich phase diagram. However, this has the artificial feature of a non dispersive level. In reality all materials have some degree of B’B’ hopping and we wish to illustrate the qualitative difference that results from this hopping. We explored two cases, $t' = 0.3$ and $t' = -0.3$ for these particle-hole asymmetric cases.

A. Monte Carlo

In Fig.11 we show the structure factor data, at two densities, for A type and C type phases, to demonstrate one remarkable difference from the particle-hole symmetric case. As we saw earlier in Fig.7 for $t' = 0$ the structure factor data were very noisy for AF phases, with many sub-dominant \mathbf{q} peaks around the central peak. The saturation value for the A-type peak in the symmetric case was $\sim 10^{-2}$, while now it is ~ 0.2 , close to the ideal value of 0.25. The sharp change in the structure factor makes the identification of the T_c scale more reliable. Although inclusion of t' does not remove the noise completely, it is reduced over a reasonable part of the phase diagram.

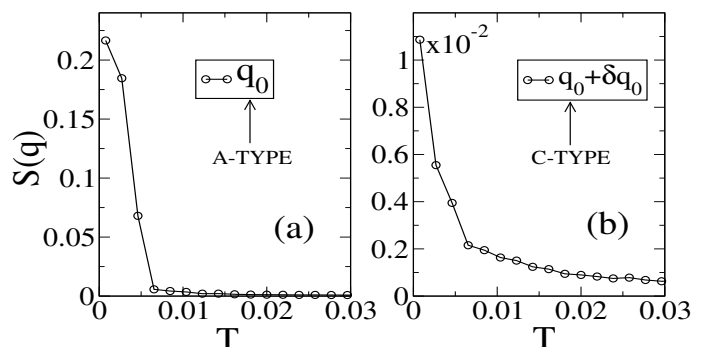


FIG. 11: $S(\mathbf{q})$ for $t' = 0.3$ and $\Delta = 0$ at (a): a typical density $n \sim 0.5$ for A-type phase and (b): a typical density $n \sim 1.2$ (this particular choice is for minimum frustration in C-type) for C type phase. A demonstration of $S(q)$ with no sub-dominant peaks, unlike at $t' = 0$.

Fig.12 presents the $n - T_c$ phase diagram for $t' = 0.3$ and $\Delta = 0$ established from Monte Carlo, along with the δE from the variational approach. For FM, the window of stability gets reduced in low density regime but enhanced at high density. The $\uparrow\uparrow\downarrow\downarrow$ phase appears again, but being a finite size artifact, is absorbed in the FM (and not shown). There is a wider space with moderate T_c for A type AF, located asymmetrically in density. The spiral and C type phases are also obtained with relatively less noise, see Fig.11, right panel. The $n - T$ phase diagram for $t' = -0.3$ and $\Delta = 0$, can be obtained from transformation $n \rightarrow 3 - n$, *i.e.*, horizontally reversing Fig.12.

B. Variational scheme

We employ the variational scheme discussed earlier and obtain the ground state phase diagram for $t' = \pm 0.3$ is shown in Fig.13. Turning on t' has a significant effect on the phase diagram, when we use the $t' = 0$ case, Fig.2 top panel, for reference. The particle hole symmetry ($n \rightarrow 3 - n$) is destroyed at finite Δ but a reduced symmetry $(n, \Delta, t') \rightarrow (3 - n, -\Delta, -t')$ still holds. The phase diagram is richer in the middle of the density window where crossing among various phases occurs at different densities. Due to the symmetry mentioned above it is enough to discuss the $\Delta > 0$ case with $t' = \pm 0.3$.

For $t' = 0.3$ the trends from MC are well reproduced by the variational scheme on large (20^3) systems at $\Delta = 0$.

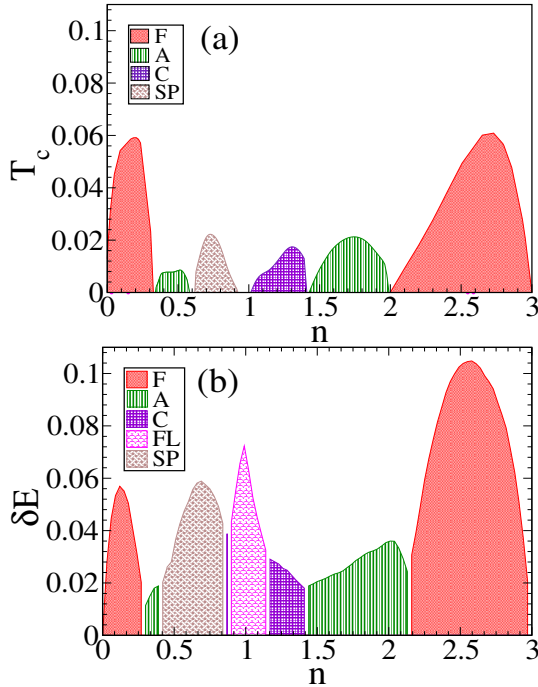


FIG. 12: Colour online: Phase diagram obtained via Monte Carlo (top) and from the variational calculation (bottom) at $t' = 0.3$ and $\Delta = 0$.

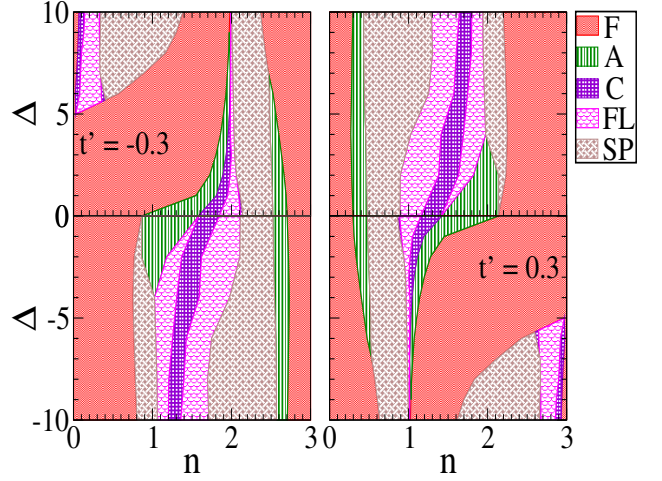


FIG. 13: Colour online: Ground state phase diagram in the presence of t' . Left panel: $t' = -0.3$. Right panel: $t' = 0.3$.

We observe reduced stability of FM at low density and enhancement at high density. **Describe the MC-varnl fig in some detail., what would happen if Δ were larger.?** Note that the overall correspondence between the Monte Carlo and the variational approach is much better here than in the $t' = 0$ case, Fig.8 and Fig.9.

The A-type phase becomes very thin in the left, but unaffected by Δ , while in right side it widens up in the low Δ and gets replaced by the spiral quickly as we go up in Δ . Flux and C-type both become stable for high Δ with a gradual shift in the high density. For $t' = -0.3$, at very small Δ in the left and the middle part A-type and the spiral are major candidates with small window for C-AF and Flux. The behaviour in this part is not very sensitive to sign of t' .

Focusing on $t' = -0.3$, as go up from $\Delta = 0$ to $\Delta \sim 5$ the AF phases become less and less stable and are almost wiped out from the left part of the density, and FM becomes stable there. The largest stability window of FM occurs roughly near $\Delta \sim 5$, where its stable upto $n \sim 1.8$. Going further with higher Δ , FM loses its stability, from C type, Flux and spirals. However, there is very thin strip of stability of the FM in the band edge in the left part, and towards the middle density, there is re-entrance of the FM phase.

In the right part of the density, we have FM, A type and spiral. Increasing Δ reduces the stability of A type to FM, making it vanish near $\Delta \sim 7$, while FM window keeps increasing with Δ .

The DOS for the ordered F, A, C, Flux phase and the paramagnet are shown in Fig.14. The dispersion of the previously localised level causes the enhancement in the bandwidth overall, because, the $m - f$ levels that hybridise are separated by Δ for all \mathbf{k} in symmetric case, whereas the separation for these level the asymmetric case is $\Delta - \epsilon'_k$, which varies from $\Delta - 12|t'|$, to $\Delta + 12|t'|$. This also reduces the band gap to smaller value than Δ . For $t' = 0.3$, FM has the largest bandwidth, with

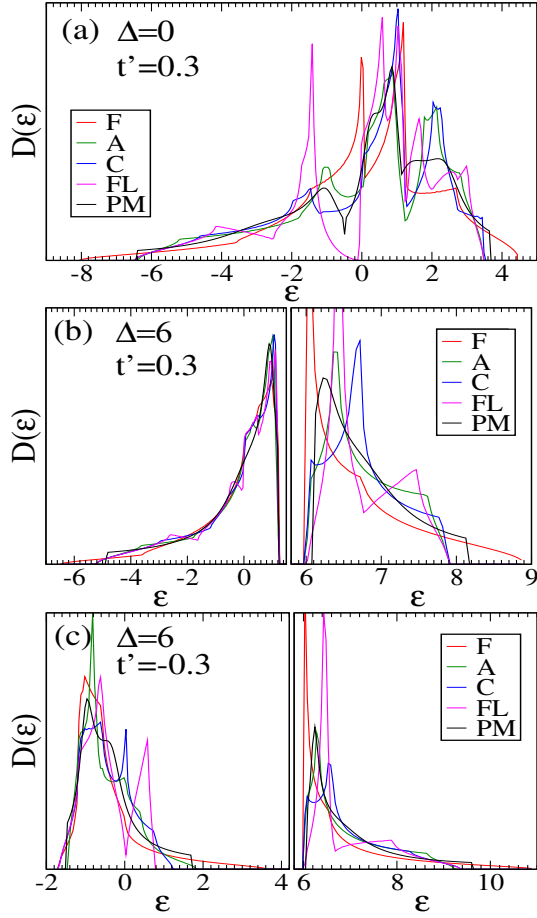


FIG. 14: Colour online: DOS for the F, A, C, FL, PM phases (a): $\Delta = 0, t' = 0.3$, there is no resemblance to the particle-hole symmetric case. FM and PM have largest bandwidth, while A, C, Flux have almost same bandwidth (b): $\Delta = 6, t' = 0.3$, due to large band-gap, two bands are shown in two different panels (left, right) the same bandwidth order, right band less effected from t' , being situated around Δ (c): $\Delta = 6, t' = -0.3$. The structure of the band edges has changed drastically. Now band edges of the FM, Flux and C type coincide on the left, while on the right edge of the first panel FM is more widespread.

paramagnet second largest. The band edges of A, C, Flux almost coincide both for small and large Δ . For $t' = -0.3$, and $\Delta = 6$ however, the situation changes. Here the lower edge of the band for FM, Flux and C coincide (panel (c), Fig.14), and the DOS of Flux, or C, is higher than FM, which explains why FM becomes unstable in the left side and taken by Flux and C, upon increasing Δ .

We also estimate the phase separation boundaries between FM, A, C phases shown in Fig.15. For $t' = 0$ and for $\Delta > 0$, we see that PS regions are significant, while they vanish for $\Delta < 0$ as we go down. For $t' = 0.3$, (right panel) the PS boundaries are too narrow to be visible.

In Fig.16 we have shown the $\delta E(n)$ calculated for 20^3 size. This shows the same qualitative trend as in Fig.12,

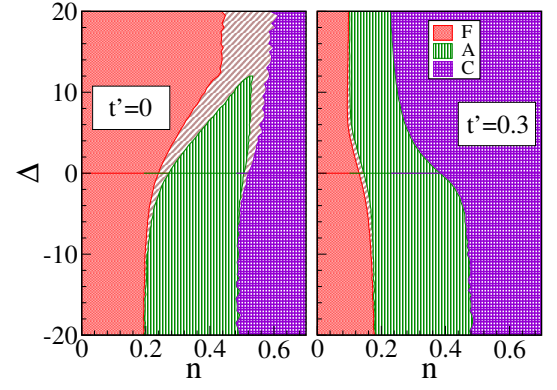


FIG. 15: Colour online: PS regions. left column for $t'=0$ and right column of $t'=0.3$. Notice that PS regions are significant for $\Delta > 0$ and $t' = 0$, for $t' \neq 0$ and for $\Delta < 0$ PS boundaries almost vanish.

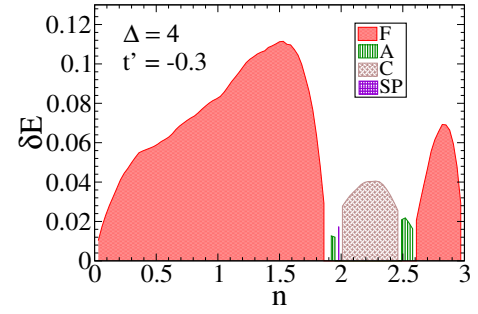


FIG. 16: Colour online: Asymmetric case, the energy difference δE of ground-state and paramagnetic phase. Top: $\Delta = 4, t' = -0.3$ where FM is stable in the large portion of the density. Bottom: $\Delta = 0, t' = 0.3$ The trends of δE match with T_c .

but the FM phase has a much larger stability window.

Summarise the qualitative effects of t' : asymm/changing phase windows, impact on T_c , the ultimate non-magnetic limit.

V. DISCUSSION

- Relevance wrt expts: comments on $T_c(x)$ and Δ dep.
- Lessons from 2D about the impact of t' , phases at large Δ .
- A better description of frustration in the itinerant context via the 2D-3D comparison.
- Any lessons from the FCC Heis AF, pertb by small J' ?
- Effect of ASD... (pm)
- Band structure, Hubbard effects ... ref to 3D Hubb based calcs (pm)
- Energy landscape.. (pm)

VI. CONCLUSIONS

Acknowledgments

We acknowledge use of the high performance computing facility at HRI. PM was supported by a DAE-SRC Outstanding Research Investigator Award, and the DST India via the Indo-EU ATHENA project.

Appendix A

Here we show how to calculate dispersion for selected ordered phases, which have relatively small unit cells. We define the unit cell for each phase, and go to k -space where the hamiltonian becomes block diagonal.

1. Spectrum for collinear phases

The Hamiltonian can be diagonalized by Fourier transformation. We write the Hamiltonian H as $H = H_0 + H_J$, where, H_0 is given by,

$$H_0 = \sum_{\vec{X}, \sigma} [\epsilon_1 f_{\vec{X}, \sigma}^\dagger f_{\vec{X}, \sigma} + \epsilon_2 m_{\vec{X}+\vec{a}_1, \sigma}^\dagger m_{\vec{X}+\vec{a}_1, \sigma}] - t' \sum_{\vec{X}, \sigma} \sum_{\vec{\delta} \in \text{NNN}} (m_{\vec{X}+\vec{a}_1, \sigma}^\dagger m_{\vec{X}+\vec{a}_1+\vec{\delta}, \sigma} + \text{h.c.}) - t \sum_{\vec{X}, \sigma} \sum_{\vec{\delta} \in \text{NN}} (f_{\vec{X}, \sigma}^\dagger m_{\vec{X}+\vec{\delta}, \sigma} + \text{h.c.}) \quad (\text{A1})$$

and H_J is given by

$$H_J = J \sum_{\vec{X}} \vec{S}(\vec{X}) \cdot \vec{\sigma}_{\alpha, \beta} f_{\vec{X}, \alpha}^\dagger f_{\vec{X}, \beta} \quad (\text{A2})$$

The lattice vector \vec{X} is defined as $\vec{X} = n_1 \vec{A}_1 + n_2 \vec{A}_2 + n_3 \vec{A}_3$ with $A_i, i = 1, 2, 3$ as the primitive lattice vectors ($A_1 = (2, 0, 0)$, $A_2 = (1, 1, 0)$, $A_3 = (0, 1, 1)$), defining the periodicity of lattice with the 2 site unit cell. With this periodicity, the unit cell has one "f" and one "m" site at

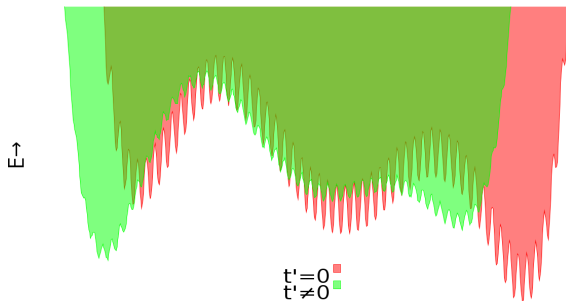


FIG. 17: Colour online: **Re-do the landscape....**

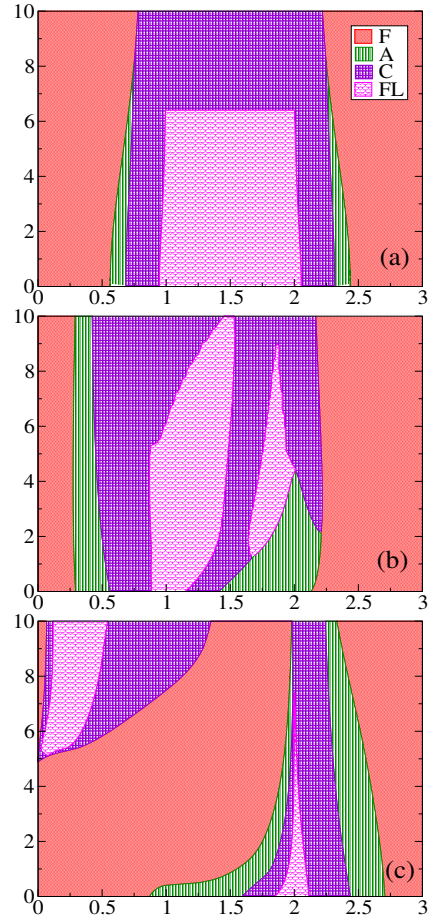


FIG. 18: Colour online: Phase diagram for $t' = 0, 0.3, -0.3$ calculated on $N = 16^3$ size using F, A, C and Flux phase.

$(0, 0, 0)$ and $(1, 0, 0)$ respectively. Now doing a Fourier transform on "f" operators (similarly for "m"s)

$$f_{\vec{X}, \sigma}^\dagger = \frac{1}{\sqrt{N}} \sum_{\vec{k}} f_{\vec{k}, \sigma}^\dagger \exp(i\vec{k} \cdot \vec{X}) \quad (\text{A3})$$

$$f_{\vec{X}, \sigma} = \frac{1}{\sqrt{N}} \sum_{\vec{k}} f_{\vec{k}, \sigma} \exp(-i\vec{k} \cdot \vec{X}) \quad (\text{A4})$$

This simplifies the non-magnetic part H_0 as follows,

$$H_0 = \sum_{\vec{k}, \sigma} [(\epsilon_2 + A'_k) m_{\vec{k}, \sigma}^\dagger m_{\vec{k}, \sigma} + \epsilon_1 f_{\vec{k}, \sigma}^\dagger f_{\vec{k}, \sigma} + (A_k f_{\vec{k}, \sigma}^\dagger m_{\vec{k}, \sigma} + \text{h.c.})] \quad (\text{A5})$$

$$= \sum_{\vec{k}, \sigma} \begin{pmatrix} f_{\vec{k}, \sigma}^\dagger & m_{\vec{k}, \sigma}^\dagger \end{pmatrix} \begin{pmatrix} \epsilon_1 & A_k \\ A_k & \epsilon_2 + A'_k \end{pmatrix} \begin{pmatrix} f_{\vec{k}, \sigma} \\ m_{\vec{k}, \sigma} \end{pmatrix} \quad (\text{A6})$$

Which is reduced to 2×2 block. the amplitudes A_k and A'_k are just the cubic and FCC dispersions given by

$$A_k = -2t(\cos k_x + \cos k_y + \cos k_z) \quad \text{and} \quad A'_k = -4t'(\cos k_x \cos k_y + \cos k_y \cos k_z + \cos k_z \cos k_x)$$

Next, we have to simplify the H_J part. For the collinear phases, $\vec{S}(\vec{X})$ can be expressed as

$$\vec{S}(\vec{X}) = \begin{pmatrix} 0 \\ 0 \\ 1 \end{pmatrix} \exp(i\vec{q} \cdot \vec{X}) \quad (\text{A7})$$

For FM, \vec{q} is trivially $(0,0,0)$. For A-type, $\vec{q} = (\frac{\pi}{2}, -\frac{\pi}{2}, \frac{\pi}{2})$, while for C-type $\vec{q} = (0, \pi, -\pi)$. Now, plugging this value of $\vec{S}(\vec{X})$ in H_J and doing the Fourier transform for the H_J , we get,

$$H_J = J \sum_{\vec{x}} \sigma f_{\vec{k},\sigma}^\dagger f_{\vec{k}+\vec{q},\sigma} \quad ; \sigma = \pm 1 \quad (\text{A8})$$

Now $\vec{q} = 0$ for FM, so H_J becomes diagonal. Thus total hamiltonian H still remains 2×2 block, and the eigenvalues for the FM are solutions of the following 2×2 block

$$H_{2 \times 2}(\vec{k}, \sigma) = \begin{pmatrix} \epsilon_1 + J\sigma & A_{\vec{k}} \\ A_{\vec{k}} & \epsilon_2 + A'_{\vec{k}} \end{pmatrix} \quad (\text{A9})$$

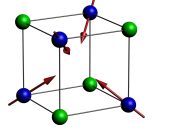
For A-type and C-type phases, we get matrix elements connecting $|\vec{k}, \sigma\rangle \rightarrow |\vec{k} + \vec{q}, \sigma\rangle \rightarrow |\vec{k}, \sigma\rangle$, so that now we get to solve following 4×4 block

$$H_{4 \times 4}(\vec{k}, \sigma) = \begin{pmatrix} \epsilon_1 & J\sigma & A_{\vec{k}} & 0 \\ J\sigma & \epsilon_1 & 0 & A_{\vec{k}+\vec{q}} \\ A_{\vec{k}} & 0 & \epsilon_2 + A'_{\vec{k}} & 0 \\ 0 & A_{\vec{k}+\vec{q}} & 0 & \epsilon_2 + A'_{\vec{k}} \end{pmatrix} \quad (\text{A10})$$

From these we obtain the spectrum for F,A,C phases on large ($\sim 100^3 - 500^3$) lattices, which can be used to calculate the density of states, phase diagram, phase separation windows etc.

2. Spectrum for the Flux phase

The unit cell for the Flux phase has $4B$, and $4B'$ atoms lying on the corners of the cube. The primitive lattice vectors become $A_i = \{(2, 0, 0), (0, 2, 0), (0, 0, 2)\}$. At finite J , the same procedure (as for collinear phases) will reduce the hamiltonian into 16×16 block. To make life a bit simple, we use the $J \rightarrow \infty$ limit on the hamiltonian for the Flux phase, which is same as used in¹⁸ except its the 3D version.



This gives us 4 spinless f_i levels and 8 $m_{i,\sigma}$ levels in the unit cell, which upon simplification reduces to 12×12 block. With the basis $(f_i(k) \ m_{i\uparrow}(k))_{i \in \{1,2,3,4\}}$ The hamiltonian breaks into 12×12 block given as follows

$$H = \begin{pmatrix} \Delta & 0 & 0 & 0 & t_{1\uparrow}a_1 & t_{1\downarrow}a_1 & t_{1\uparrow}a_2 & t_{1\downarrow}a_2 & 0 & 0 & t_{1\uparrow}a_3 & t_{1\downarrow}a_3 \\ 0 & \Delta & 0 & 0 & t_{2\uparrow}a_2 & t_{2\downarrow}a_2 & t_{2\uparrow}a_1 & t_{2\downarrow}a_1 & t_{2\uparrow}a_3 & t_{2\downarrow}a_3 & 0 & 0 \\ 0 & 0 & \Delta & 0 & t_{3\uparrow}a_3 & t_{3\downarrow}a_3 & 0 & 0 & t_{3\uparrow}a_2 & t_{3\downarrow}a_2 & t_{3\uparrow}a_1 & t_{3\downarrow}a_1 \\ 0 & 0 & 0 & \Delta & 0 & 0 & t_{4\uparrow}a_3 & t_{4\downarrow}a_3 & t_{4\uparrow}a_1 & t_{4\downarrow}a_1 & t_{4\uparrow}a_2 & t_{4\downarrow}a_2 \\ t_{1\uparrow}^*a_1 & t_{2\uparrow}^*a_2 & t_{3\uparrow}^*a_3 & 0 & 0 & 0 & t_{12} & 0 & t_{23} & 0 & t_{13} & 0 \\ t_{1\downarrow}^*a_1 & t_{2\downarrow}^*a_2 & t_{3\downarrow}^*a_3 & 0 & 0 & 0 & 0 & t_{12} & 0 & t_{23} & 0 & t_{13} \\ t_{1\uparrow}^*a_2 & t_{2\uparrow}^*a_1 & 0 & t_{4\uparrow}^*a_3 & t_{12} & 0 & 0 & 0 & t_{13} & 0 & t_{23} & 0 \\ t_{1\downarrow}^*a_2 & t_{2\downarrow}^*a_1 & 0 & t_{4\downarrow}^*a_3 & 0 & t_{12} & 0 & 0 & 0 & t_{13} & 0 & t_{23} \\ 0 & t_{2\uparrow}^*a_3 & t_{3\uparrow}^*a_2 & t_{4\uparrow}^*a_1 & t_{23} & 0 & t_{13} & 0 & 0 & 0 & t_{12} & 0 \\ 0 & t_{2\downarrow}^*a_3 & t_{3\downarrow}^*a_2 & t_{4\downarrow}^*a_1 & 0 & t_{23} & 0 & t_{13} & 0 & 0 & 0 & t_{12} \\ t_{1\uparrow}^*a_3 & 0 & t_{3\uparrow}^*a_1 & t_{4\uparrow}^*a_2 & t_{13} & 0 & t_{23} & 0 & t_{12} & 0 & 0 & 0 \\ t_{1\downarrow}^*a_3 & 0 & t_{3\downarrow}^*a_1 & t_{4\downarrow}^*a_2 & 0 & t_{13} & 0 & t_{23} & 0 & t_{12} & 0 & 0 \end{pmatrix}$$

Where the symbols in the above are defined as $\alpha = \sqrt{\frac{\sqrt{3}+1}{2\sqrt{3}}}$; $\beta = \sqrt{\frac{\sqrt{3}-1}{2\sqrt{3}}}$; $z = \frac{1-i}{\sqrt{2}}$

$$a_1 = 2 \cos k_1; \quad a_2 = 2 \cos k_2; \quad a_3 = 2 \cos k_3; \quad t_{12} = -4t' \cos k_1 \cos k_2; \quad t_{23} = -4t' \cos k_2 \cos k_3; \\ t_{13} = -4t' \cos k_1 \cos k_3; \quad t_{1\uparrow} = t_{2\uparrow} = -t\alpha; \quad t_{3\uparrow} = t_{4\uparrow} = -t\beta; \quad t_{1\downarrow} = -t_{2\downarrow} = tz\beta; \quad t_{3\downarrow} = -t_{4\downarrow} = -tz^*\alpha$$

¹ For reviews, see D. D. Sarma, Current Op. Solid St. Mat. Sci.,**5**, 261 (2001), D. Serrate, J. M. de Teresa and M. R.

Ibarra, J. Phys. Cond. Matt. **19**, 023201 (2007).

- ² Mark T. Anderson, Kevin B. Greenwood, Gregg A. Taylor, and Kenneth R. Poeppelmeier. *Progress in Solid State Chemistry*, 22, 197 (1993).
- ³ K.-I. Kobayashi, T. Kimura, H. Sawada, K. Terakura, and Y. Tokura. *Nature (London)* 395, 677, (1998).
- ⁴ M.A. Subramanian N.S. Rogado, J. Li. *Advances in Materials* 17, 2225 (2005).
- ⁵ Hena Das, Umesh V. Waghmare, T. Saha-Dasgupta, and D. D. Sarma. *Phys. Rev. Lett.* 100, 186402, (2008).
- ⁶ Hena Das, Molly De Raychaudhury, and T. Saha-Dasgupta. *Appl. Phys. Lett.* 92, 201912 (2008).
- ⁷ D. D. Sarma, Priya Mahadevan, T. Saha-Dasgupta, Sugata Ray, and Ashwani Kumar. *Phys. Rev. Lett.* 85, 2549 (2000).
- ⁸ J. B. Philipp, P. Majewski, L. Alff, A. Erb, R. Gross, T. Graf, M. S. Brandt, J. Simon, T. Walther, W. Mader, D. Topwal, and D. D. Sarma. *Phys. Rev. B* 68, 144431 (2003).
- ⁹ P. Majewski, S. Geprägs, A. Boger, M. Opel, A. Erb, R. Gross, G. Vaitheeswaran, V. Kanchana, A. Delin, F. Wilhelm, A. Rogalev, and L. Alff. *Phys. Rev. B* 72, 132402 (2005).
- ¹⁰ Y. Krockenberger, K. Mogare, M. Reehuis, M. Tovar, M. Jansen, G. Vaitheeswaran, V. Kanchana, F. Bultmark, A. Delin, F. Wilhelm, A. Rogalev, A. Winkler, and L. Alff. *Phys. Rev. B* 75, 020404 (2007).
- ¹¹ Tapas Kumar Mandal, Claudia Felser, Martha Greenblatt, and Jürgen Kübler. *Phys. Rev. B* 78, 134431 (2008).
- ¹² A. Chattopadhyay and A. J. Millis. *Phys. Rev. B* 64, 024424 (2001).
- ¹³ K. Phillips, A. Chattopadhyay, and A. J. Millis. *Phys. Rev. B* 67, 125119 (2003).
- ¹⁴ M. Hamada and H. Shimahara. *Phys. Rev. B* 51, 3027 (1995).
- ¹⁵ D. F. Agterberg and S. Yunoki. *Phys. Rev. B* 62, 13816 (2000).
- ¹⁶ J. L. Alonso, J. A. Capitán, L. A. Fernández, F. Guinea, and V. Martín-Mayor. *Phys. Rev. B* 64, 054408 (2001).
- ¹⁷ K. Pradhan and P. Majumdar, *Europhys. Lett.* **85**, 37007 (2009).
- ¹⁸ Prabuddha Sanyal and Pinaki Majumdar. *Phys. Rev. B* 80, 054411 (2009).
- ¹⁹ Sanjeev Kumar and Pinaki Majumdar. *EPJ B* 50, 571 (2006).
- ²⁰ Prabuddha Sanyal, Hena Das, and T. Saha-Dasgupta. *Phys. Rev. B* 80, 224412 (2009).
- ²¹ Shuai Dong, Rong Yu, Seiji Yunoki, J.-M. Liu, and Elbio Dagotto. *Phys. Rev. B* 78, 155121 (2008).
- ²² We have worked on $\Delta \in [-10, 10]$, so J has to be large compared to it. We used $J = 1000$, as the atomic bands which, for finite J , are actually dispersive (of band-width $\sim \mathcal{O}(\frac{1}{\Delta})$) become actually atomic to required numerical accuracy.
- ²³ We compared ratio of the maximum of $(\delta E)^{FM}$ and maximum of $(\delta E)^{AF}$ in the density window, for $\Delta = 0$ and $t' = 0$